RESEARCH ARTICLE

NANO · MICRO small
www.small-journal.com

Validating the Virtual Calendering Process With 3D-Reconstructed Composite Electrode: An Optimization Framework for Electrode Design

Jaejin Lim, Jihun Song, Kyung-Geun Kim, Jin Kyo Koo, Hyobin Lee, Dongyoon Kang, Young-Jun Kim, Joonam Park, and Yong Min Lee**

Calendering is an essential fabrication step for lithium-ion battery electrodes, aimed at achieving the target density through mechanical compression. During this process, the electrode's microstructure significantly deforms, affecting its electrochemical performance. Therefore, it is important to understand how the microstructure evolves during calendering and correlate these changes with electrochemical behavior. Despite tremendous experimental efforts, there are limitations in obtaining sufficient outcomes. In this regard, simulations offer valuable information; however, the highest priority is to develop a reliable modeling framework that reflects actual microstructural changes and establish a robust validating methodology. Without such a framework, computational predictions may not align with experimental results. This study develops a virtual calendering framework based on high-resolution FIB-SEM tomography images of a bimodal $LiNi_{0.6}Co_{0.2}Mn_{0.2}O_2$ cathode with a mass loading of 19.8 mg cm^{-2} and 96 wt.% active material. The framework is rigorously validated through systematically designed experiments across various electrode densities (2.3–4.0 g cm^{-3}) and further analysis of hidden microstructural features, such as ionic tortuosity, contact area, and crack structure through additional tomography analysis. The virtual calendering framework successfully predicts microstructural changes and electrochemical performance, offering a reliable pathway for identifying optimal design parameters in a time- and cost-effective manner.

1. Introduction

Lithium-ion batteries (LIBs) have already played a pivotal role in the electrified world as movable energy-storage devices, ranging from portable electronics to electric vehicles, owing to their superior energy density, long cycle life, and affordability.[1] However, the demand for higher energy density and better life cycle of LIBs is still met by discovering new electrode or electrolyte materials and optimizing electrode design or fabrication process. In particular, when the materials and design parameters for slurry coating and drying are set, calendering must be the most important process in determining the volumetric energy density and electrochemical performance of LIBs.[2,3]

Specifically, an increase in the electrode density can augment the contact area between the electrode components: active materials, conductive additives, and binders. In other words, the additional electronic conduction pathways caused by the calendering process can lead to a decrease in the bulk resistivity of the composite electrodes.[4–7] Moreover, increased contact between the binders and other electrode components can strengthen the mechanical robustness of the composite electrodes for long-term reliability.[8] However, as the electrode density increases through the calendaring process, the volume fraction of the pore domains filled with the electrolyte decreases, hindering Li-ion diffusion and migration. Furthermore, as the connectivity of the pores becomes more tortuous, the rate capability of the composite electrodes deteriorates substantially.[9] A more concerning

J. Lim, D. Kang, Y. M. Lee
Department of Chemical and Biomolecular Engineering
Yonsei University
50 Yonsei-ro, Seodaemun-gu, Seoul 03722, Republic of Korea
E-mail: yongmin@yonsei.ac.kr

J. Lim, H. Lee, D. Kang, Y. M. Lee
Department of Energy Science and Engineering
Daegu Gyeongbuk Institute of Science and Technology (DGIST)
Daegu 42988, Republic of Korea

J. Song, K.-G. Kim
Energy Science and Engineering Research Center
Daegu Gyeongbuk Institute of Science and Technology (DGIST)
Daegu 42988, Republic of Korea

J. K. Koo, Y.-J. Kim
SKKU Advanced Institute of Nano Technology (SAINT)
Sungkyunkwan University
Suwon 16419, Republic of Korea

J. Park
Gwacheon R&D Campus
LG Energy Solution
Gyeonggi-Do 13818, Republic of Korea
E-mail: joonam.park@lgensol.com

The ORCID identification number(s) for the author(s) of this article can be found under https://doi.org/10.1002/smll.202410485

DOI: 10.1002/smll.202410485

issue is crack formation in the electrode active materials during the calendaring process when the compression ratio is high,[10–12] that is, the locally concentrated stress exceeds the compression strength of the active materials. In other words, more cracks lead to electrochemically inactive electrode particles and an enlarged surface of the active materials exposed to the electrolyte, where irreversible decomposition of electrolytes can occur, thereby decreasing the cell capacity and increasing the resistance at the interfaces.[13–15] As a result, the electrode density should be carefully optimized to secure not only the rate performance but also the long-term reliability of LIB cells.[16–20]

Many previous studies on the effect of electrode density have focused on the experimental correlation between the compression ratio and electrochemical performance.[21–23] However, analyzing and quantifying the morphological parameters such as porosity, pore size distribution, tortuosity, interparticle contact area, and particle crack formation through experimental analysis is difficult.[24–27] Hence, to deep-dive the design parameters and electrochemical properties of electrodes, computational analysis via physical-based modeling and simulation must be a strong alternative.[28–31]

Lenze et al. utilized a pseudo-2D (P2D) model to obtain the morphological and electrochemical parameters of cathodes under different calendering conditions, which was highly efficient in terms of computational resources. Specifically, they performed parameter fitting to match experimental and simulation results.[32] However, fitting the morphological parameters solely based on electrochemical tests, such as the rate test, for a model that incorporates both morphological and electrochemical parameters may lead to over- or under-estimation of the parameters. A digitally twinned microstructural electrode, which fully mimics the morphology of the porous structure, is one of the best solutions.[33–36] Lu et al. implemented the 3D reconstruction of electrodes using X-ray nano-computed tomography (CT) to analyze the correlation between the porosity and tortuosity factor with respect to the compression level. Moreover, they experimentally validated the simulated discharge performance of the electrode before and after the calendaring process to determine the impact of the electrode microstructure on electrochemical performance.[37] However, due to the difficulty of preparing electrode samples and creating corresponding high-resolution 3D structures, microstructural analysis is a laborious task while changing design parameters such as electrode density.

To reduce the difficulty in gathering tomographic images appropriately, simulations that generate a virtual electrode structure and imitate its compression using open-source codes or commercial tools such as LAMMPS, LIGGGHTS, MATBOX, GeoDict, and EDEM have been reported.[38–42] Nikpour et al. suggested a multiphase smoothed particle (MPSP) model based on the discrete element method (DEM) to reflect the actual nonuniform particle distribution and simulate the interplay between particles before and after the calendaring process.[43] Ngandjong et al. attempted to make the electrode structure that undergoes the electrode manufacturing process using the coarse grain molecular dynamics (CGMD). They also simulated the electrochemical impedance, galvanostatic discharge capacity, and state of lithiation of the calendered composite electrodes.[44] However, these previous studies simplified the electrode structures with assumptions such as perfectly spherical particles, which cannot reflect the substantial effect of the surface morphology of particles on the electrochemical characteristics and ion transport in composite electrodes. Additionally, although crack formation and propagation have been highlighted as key degradation factors in secondary-particle-type active materials, the aforementioned models have not been sufficiently validated with experimental data and did not estimate how much breakage of particles occurred during calendering.

Thus, developing sophisticated microstructures of uncompressed composite electrodes and replicating the calendering process is essential. In this study, high-resolution microstructures of composite cathodes with bimodal $LiNi_{0.6}Co_{0.2}Mn_{0.2}O_2$ (NCM622) particles were created before and after the calendaring process using thousands of tomographic images from FIB-SEM measurements. Subsequently, the initial digitally twinned electrode before calendering was utilized to simulate the virtual calendering process to provide various estimations of the morphological and electrochemical properties of density-controlled composite electrodes. Finally, a virtually compressed electrode obtained from the simulation was compared with an actual calendered electrode. In addition, various experiments were conducted to validate the simulated parameters of virtual microstructures. This novel approach is expected to be a platform to analyze the reliable morphological parameters of composite electrodes.

2. Results and Discussion

We first fabricated an electrode with a loading level of 19.8 mg cm^{-2} and an electrode density of 2.3 g cm^{-3} and calendered it to the targeted electrode densities from 2.4 to 4.0 g cm^{-3}. (2.4, 2.5, 2.7, 2.8, 3.0, 3.3, 3.4, 3.5, 3.6, 3.8, and 4.0 g cm^{-3}, 11 cases in total). And then, we measured the electronic conductivity and adhesion strength of each electrode using a multiprobe conductivity analyzer and a microblade cutting system, respectively. As summarized in Figure S1a,b (Supporting Information), as the electrode was calendered further, both the electronic conductivity and adhesion strength tended to increase. For instance, the electronic conductivity could be enhanced by ca. 130% from the uncalendered state of 2.3 g cm^{-3} to fully calendered one of 4.0 g cm^{-3}. Under the same calendering condition, the adhesion strength was more significantly improved by ca. 199%. These experimental results are readily acceptable and useful to optimize electrode design parameters for application purposes, because the higher electronic conductivity and adhesion strength can lead to better power capability and longer cycling stability, respectively.

To experimentally confirm this, two electrochemical tests of the rate capability and cycle life were conducted using 2032 coin-type cells. As shown in **Figure 1a**, less calendered electrodes (<3.0 g cm^{-3}) show worse capacity at 1 C than the other highly calendered ones, which implies that uncalendared electrodes do not have sufficient electronic contacts among electrode components especially for high-rate performance. However, highly calendered electrodes of 3.8 and 4.0 g cm^{-3} exhibited lower capacity at 5 C than that of the electrode of 3.6 g cm^{-3}, which cannot be explained by the enhancement of electronic conductivity. As discussed in many previous studies, this result must be ascribed to insufficient pore volume and poor pore connectivity for lithium-ion mass transfer. In addition, the reduced contact area between the electrode active materials and the liquid electrolyte

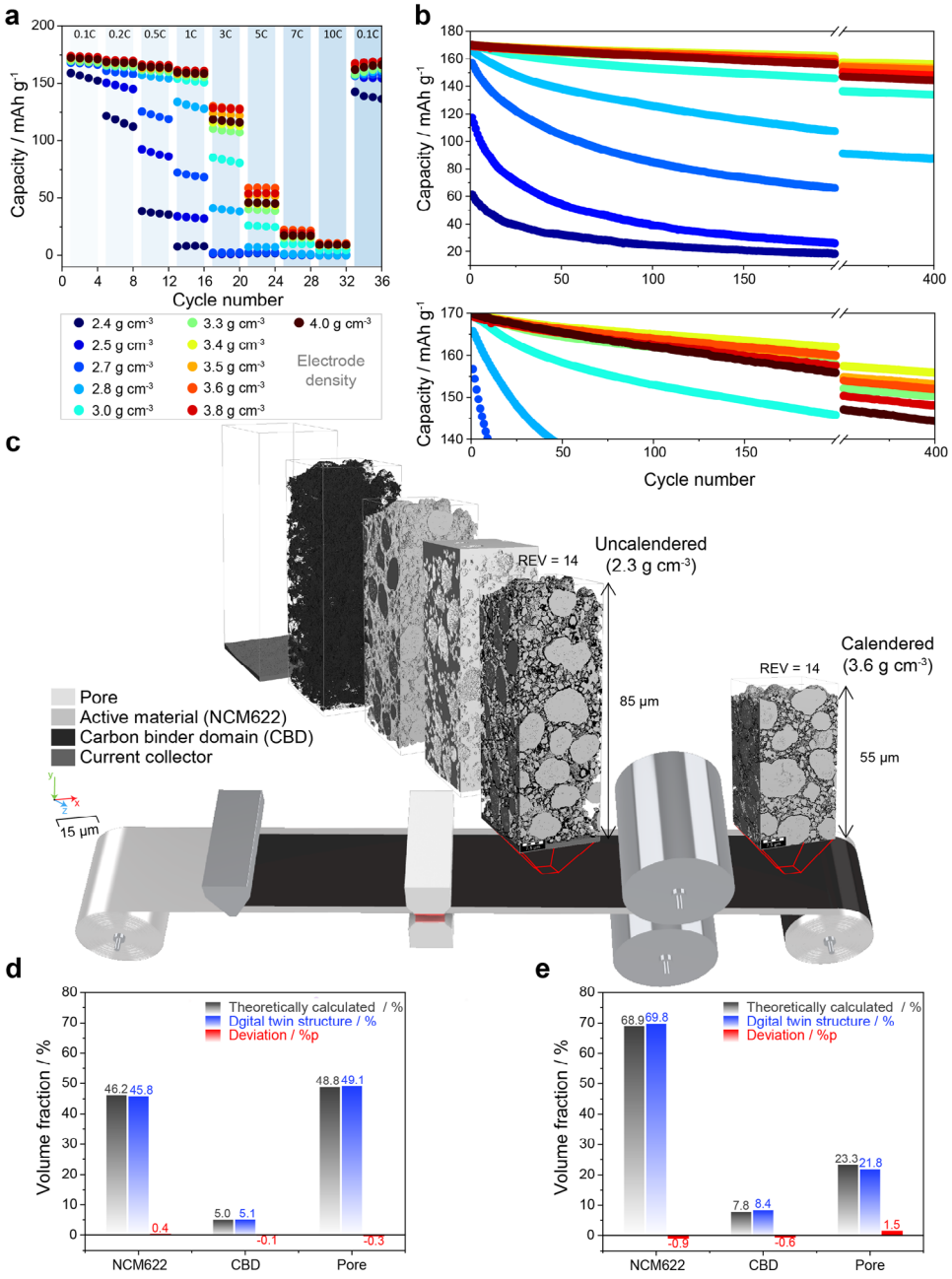

Figure 1. Electrochemical performance of composite electrode with different densities and reconstructed microstructure for the virtual calendering framework. a) Rate capability and b) cycle performance of Gr||NCM622 full cells with different cathode densities. c) Schematic of the calendering process and digitally twinned structures before and after calendering, reconstructed from FIB-SEM tomographic images. Volume fractions of each electrode component, theoretically calculated and estimated from digitally twinned electrode structures for d) uncalendared and e) calendered (3.6 g cm^{-3}) electrode.

in highly calendered electrodes results in a worse rate capability under high C-rate conditions. Physical parameters like pore tortuosity and active surface area of active materials are useful to explain the poor rate capability of highly calendered electrodes. For example, it is possible to obtain the tortuosity value of a composite electrode by conducting electrochemical impedance spectroscopy (EIS) analysis with a symmetric cell,[45–47] and the apparent surface area of the electrode materials can be measured using the Brunauer-Emmett-Teller (BET) analyzer.[48] However, it is difficult to separate the lithium-ion movement in the separator and electrode, and the latter cannot identify the electrochemically active surface areas of the composite electrodes. Thus, digitally twinned microstructure of the composite electrode can provide more accurate tortuosity or active surface area values.[34]

Figure 1b displays the capacity retention curves as a function of the cycle number at 0.5 a CC/CV charge of 0.5 C CC discharge.

The capacity of an electrode with a density of 2.8 g cm^{-3} was reduced to less than half of its initial capacity after 400 cycles, and the electrodes with lower densities than 2.8 g cm^{-3} deteriorated even faster and could not withstand 300 cycles. These results may be explained by the insufficient adhesion strength of the less-calendered electrodes, which implies that the calendering process is essential for securing sufficient adhesion points for long-term cyclability, as well as well-developed electronic conduction pathways. Securing a capacity retention above 80% after 400 cycles, the electrode of 3.0 g cm^{-3} can be a benchmark for calendering process in this electrode design. To closely compare the capacity retention behavior of the highly calendered electrodes, Figure 1b is magnified in the y-axis range of 140–180 mAh g^{-1}. The electrode of 3.4 g cm^{-3} shows the best capacity retention of 91.9% at the 400th cycle. However, as the electrode density increases beyond 3.4 g cm^{-3}, the capacity retention tends to decrease, which is known to be closely related to the crack formation of secondary particle-type active materials during excessive calendering from previous works.[10–12] In other words, as the electrode density increases, more cracks initially form in the electrode, and they gradually propagate to consume not only organic solvents but also lithium ions to form the cathode–electrolyte interphase during cycling.[13–15] Thus, analyzing calendering-induced cracks in the electrode can be a good indicator for predicting the cycle life of electrodes. In this sense, the digital-twin-based microstructural analysis is an effective and impactful method for quantifying the cracked volume in a cycled or degraded electrode.

From this point of view, we generated two digital-twinned structures of uncalendered (2.3 g cm^{-3}) and calendered (3.6 g cm^{-3}) electrodes through reconstructing thousands of FIB-SEM tomographic images of each electrode (Figures S2–S4, Supporting Information). The reason why the density of 3.6 g cm^{-3} was chosen is that the corresponding electrode showed well-balanced rate and cycle performances. Figure 1c displays two reconstructed electrode microstructures before and after calendering, where the uncalendared electrode structure of 2.3 g cm^{-3} density and 85 μm thickness densified to have 3.6 g cm^{-3} and 55 μm. Once the digital-twin structure of the composite electrode is created, validating the reliability of structures is necessary. Therefore, we performed a comparative analysis with the representative element volume (REV), an index of whether the domain size of the digitally twinned structure was large enough to represent the entire sample, and the volume fraction of each component. Fortunately, both digital-twinned electrodes showed REV values of 14.1 and 13.9, respectively, which are much higher than the minimum required value of 5; many 3D structure studies have suggested that the REV should be higher than 5 for reliable analysis.[49,50] In addition, the volume fractions of NCM622, CBD, and the pores in the electrode structure were compared with the theoretically calculated values based on the electrode design parameters. All deviation values were lower than 2%, which is a practically acceptable level compared to previous digital-twin electrode studies (Figure 1d,e).[34]

Thus, the virtual calendering simulation could be done with the well-reconstructed electrode structure (uncalendered, 2.3 g cm^{-3}) as the initial one like **Figure 2a**, where selected eight virtually calendered electrodes (2.5, 2.8, 3.3, 3.4, 3.5, 3.6, 3.8, and 4.0 g cm^{-3}) are shown with the reconstructed calendered electrode structure (3.6 g cm^{-3}) as an answer sheet. Virtual calendering was performed using a strain-controlled compression simulation with the ElastoDict module in GeoDict 2023. In the simulation, uncalendared structure was compressed to the targeted electrode densities ranging from 2.4 to 4.0 g cm^{-3} (2.4, 2.5, 2.7, 2.8, 3.0, 3.3, 3.4, 3.5, 3.6, 3.8, and 4.0 g cm^{-3}, for a total of 11 cases). During the process, an object's voxels with stronger mechanical properties push neighboring voxels with weaker mechanical properties or occupy pore voxels, similar to the actual calendering process. Our virtual calendering successfully simulated the surface deformation of the ductile aluminum current collector owing to the high mechanical strength of the NCM 622 particles, which is commonly observed in highly calendered electrodes.[51] In contrast, the top surface of the virtually calendered electrode seems too flat compared to that of reconstructed electrode calendered by 3.6 g cm^{-3}, because our strain-controlled simulation could not reflect the spring-back phenomenon occurred during actual calendering processes. Nonetheless, fortunately, key morphological parameters like porosity and effective electronic conductivity of virtually calendered electrode of 3.6 g cm^{-3} are found to be similar to those of reconstructed electrode calendered to the same density (17.9% vs 18.7% and 1.8 S m^{-1} vs 1.9 S m^{-1}, respectively; Figure S5, Supporting Information). In addition, to confirm the reliability of our calendering simulation, porosity values obtained from virtually calendered electrodes were compared with theoretical ones like Figure 2b, where both values were well matched each other <10% error. Similarly, when effective electronic conductivities simulated from virtually calendered electrodes were compared with experimentally measured ones, both data showed quite similar values with an average relative error of ≈3.5% (Figure 2c).

Thanks to the high reliability of the virtually calendered electrode structures, we could appropriately estimate other veiled morphological parameters, such as the pore tortuosity for ionic transfer (hereafter referred to as ionic tortuosity), the specific surface area of NCM (i.e., contact area between pores and active materials), and the specific contact area between active materials and CBDs like Figure 2d–f, respectively. Since the actual electrode of 3.6 g cm^{-3} was already reconstructed, the accuracy of virtually calendered electrode in the same density can be further confirmed by high similarity of those three parameters in both electrode structures (2.5 vs 2.6 in ionic tortuosity, 7.04×10^5 vs 6.98×10^5 m^2 m^{-3} in specific surface area of active materials, and 8.74×10^5 vs 8.63×10^5 m^2 m^{-3} in the specific contact area between active materials and CBDs, reconstructed vs virtually calendered). More specifically, the ionic tortuosity significantly increased beyond the range of 3.5 to 3.6 g cm^{-3}, where the best rate capability was observed in Figure 1a. However, regardless of the increased electrode density to more than 3.3 g cm^{-3}, the specific surface area of active materials almost saturated to 6.90×10^5 m^2 m^{-3}, which may be explained by pore downsizing beyond a certain density point while maintaining contacts between active materials and pores. Consequently, we can assume that the poor rate capability of 3.8 and 4.0 g cm^{-3} electrodes is related to limited ionic transport rather than reduced reaction sites. Additionally, the specific contact area between the active materials and the CBD gradually increased with calendering because the solid materials in the electrode were closely packed for greater contact. In this sense, this parameter can support an increase in not only the effective electronic conductivity in Figure 2c but also

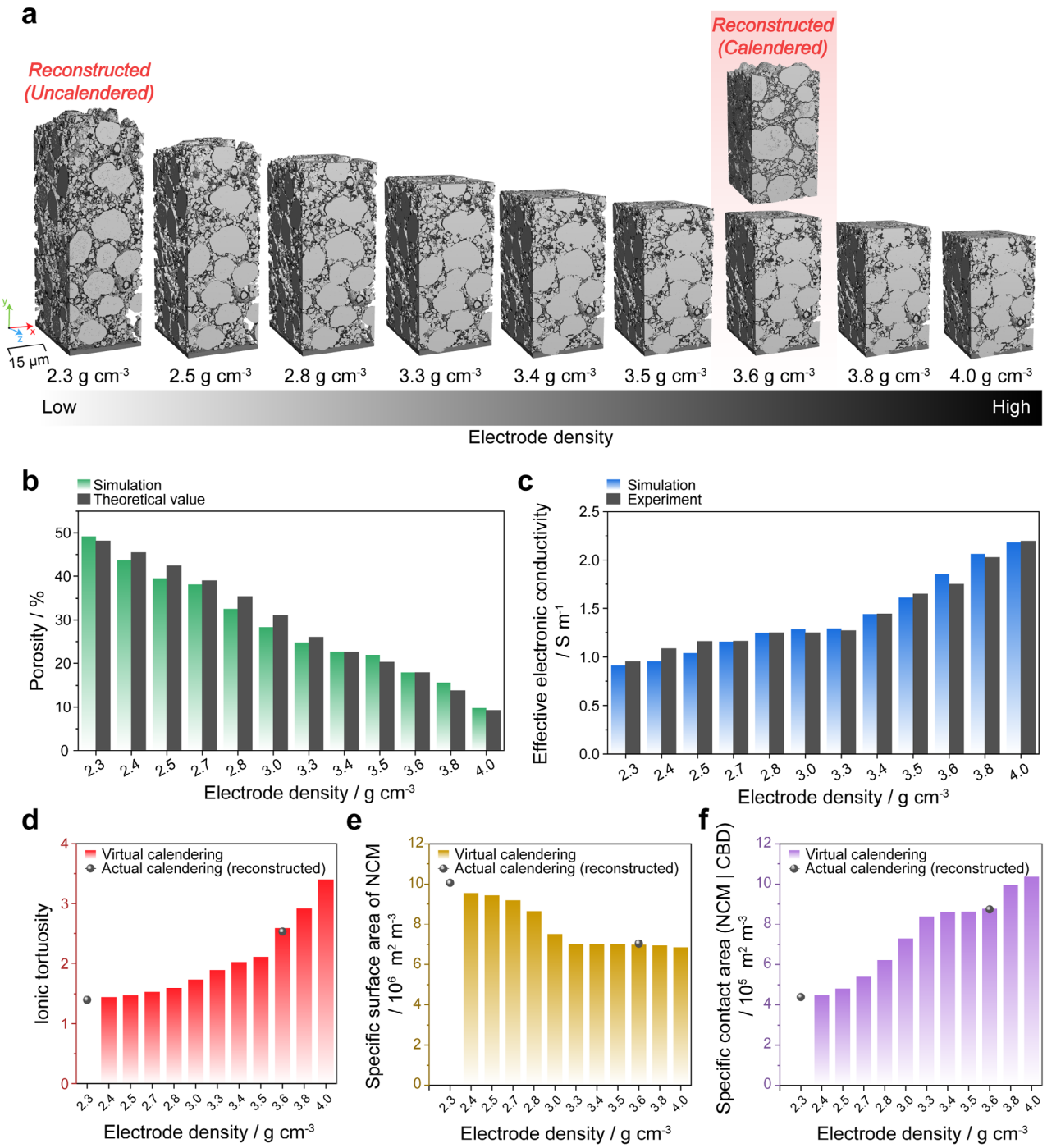

Figure 2. Changes in microstructural and electrochemical properties change with varying electrode densities. a) Schematic of the virtual calendering process. b) Porosity changes with varying densities, theoretically calculated and obtained from a virtual calendering process. c) Effective electronic conductivity of electrodes from experiments and virtual calendering process. d) Ionic tortuosity, e) specific surface area of NCM active material (specific contact area between NCM and pore), and f) specific contact area between NCM and conductive binder domain (CBD), calculated from virtual calendering structures and actual (or reconstructed) calendering structures.

the adhesive strength in Figure S1 (Supporting Information). Interestingly, a closer examination of Figure 2f reveals that the specific contact area exhibits a more complex behavior compared to other microstructural parameters. Specifically, the specific contact area remains nearly constant between electrode densities of 3.3 and 3.6 g cm^{-3} but increases sharply at 3.8 g cm^{-3}. This sudden increase appears to correspond to the formation of new contact between the active material and the CBD, a reduction in pore volume, and a rearrangement of the active materials, as shown in Figure S6 (Supporting Information), particularly at higher

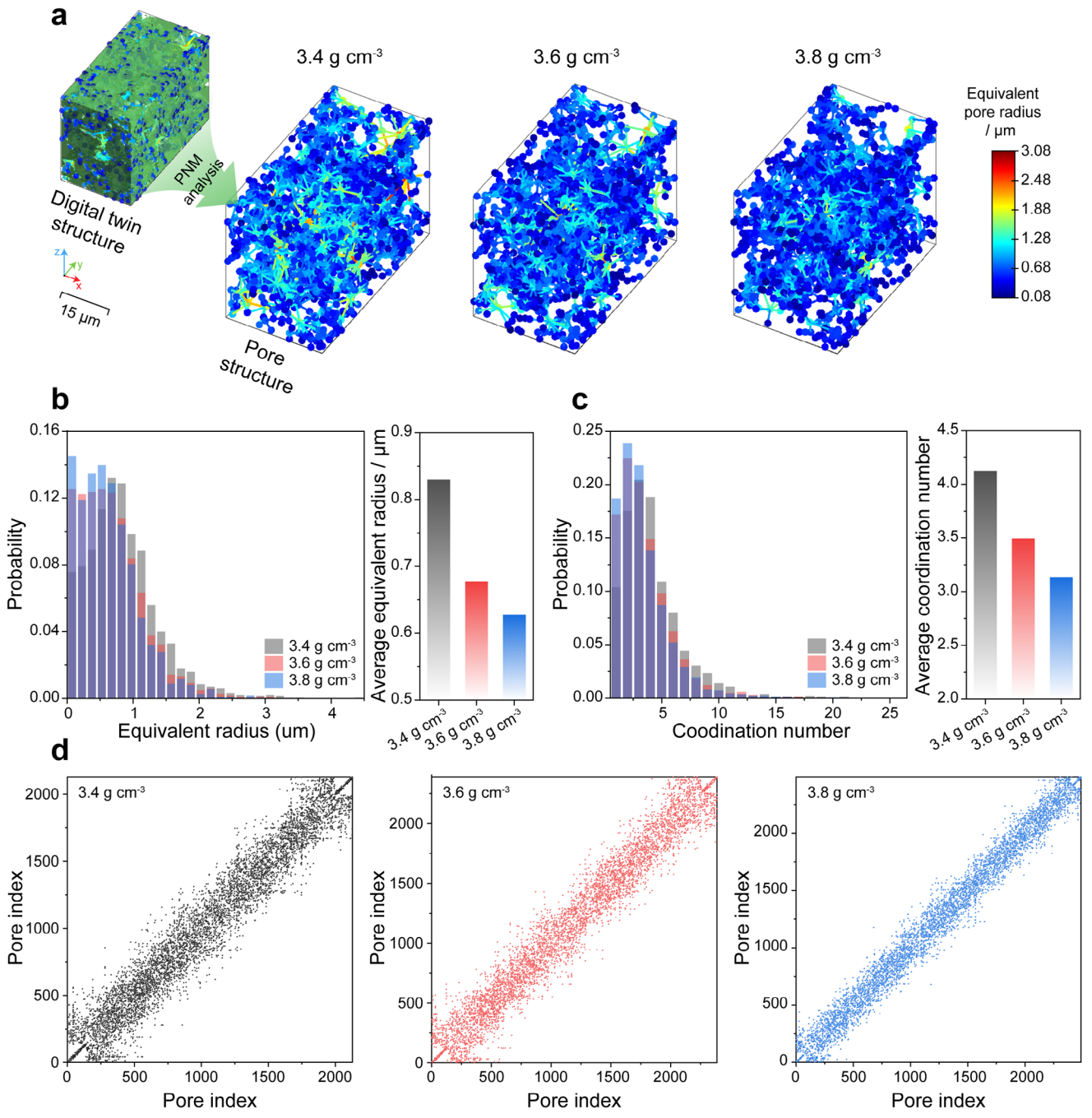

Figure 3. Pore network analysis based on the virtual calendering framework. a) Pore network structure visualized using ball (pore) and stick (connection) diagram for electrodes with densities 3.4, 3.6, and 3.8 g cm^{-3}. b) Equivalent pore radius distribution and average equivalent pore radius. c) Pore coordination number distribution and average pore coordination number, with probability representing the normalized frequency of each coordination number. d) Pore connectivity matrices for assessing overall pore connectivity.

electrode densities (beyond 3.8 g cm^{-3}). This behavior is likely attributable to the transition from a moderately close-packed structure observed at densities above 3.3 g cm^{-3} to a more densely packed configuration at elevated electrode densities. Among the three parameters discussed, the ionic tortuosity seems to determine the rate performance, as summarized in Figure 1a. Thus, deep diving of the pore structures of each calendered electrode is recommended.

Figure 3 presents the pore-quantified analysis results for electrodes with varying densities (3.4, 3.6, and 3.8 g cm^{-3}). First, the equivalent radius and connectivity of the pores were calculated using a pore network model (PNM) and visualized as a 3D

volume image (Figure 3a). As the electrode density increased, the proportion of reddish balls, which indicated larger pores, decreased along with the number of sticks connecting them. For example, the average equivalent radius of the electrode with a density of 3.8 g cm^{-3} is 25% smaller than that of the electrode with a density of 3.4 g cm^{-3} (Figure 3b). The ionic pathways through pores depicted as sticks in Figure 3a can be described by the pore coordination number, which refers to the number of connected adjacent pores. This coordination number also decreases as electrode density increases; coordination number decreases by 0.5 when electrode density increases by 0.2 g cm^{-3} under these design conditions (Figure 3c). A more detailed distribution of coordination number as a function of electrode density is presented in Figure S7 (Supporting Information). Additionally, the changes in average equivalent radius and average coordination number, from 2.3 g cm^{-3} to 4.0 g cm^{-3}, are summarized in Figure S8 (Supporting Information). Moreover, the overall pore connectivity of each electrode can be visualized by extracting each individual pore from the electrode and determining its connectivity as shown in Figure 3d. In more detail, each pore is assigned a unique number or index based on its spatial position in Cartesian coordinates. If two pores are connected, two dots are placed at the coordinates corresponding to these pore indices; for instance, if pores 3 and 5 are connected, the dots are placed at coordinates (3,5) and (5,3) (Figure S9, Supporting Information). In general, spatially adjacent pores have a higher probability of connection, resulting in a diagonal line shape in the connectivity matrix. In addition, if connectivity exists between spatially distant pores, the bandwidth of the diagonal line increases. As shown in Figure 3d, with increasing electrode density, the number of pores and the maximum pore index increased as larger pores were divided into smaller ones, resulting in a narrower diagonal bandwidth. These findings indicate that the calendaring process causes micro-sized pores to break down into nano-sized pores, making the ionic pathways between them more tortuous or, in some cases, blocked, thereby hindering pore connectivity. The connectivity data can also be represented as a normal distribution, as shown in Figure S10 (Supporting Information), indicating that electrodes with higher density have a lower standard deviation, which reflects a narrower pore connectivity.

Another benefit of virtual calendering is its ability to calculate or visualize the von Mises stress (VMS) within the composite electrodes, as shown in **Figure** 4a. As the electrode density increased, the VMS of the active materials increased, particularly at the interparticle contact points where particles were compressed against each other. Furthermore, as the electrode density increased, high VMS levels were observed not only on the particle surfaces but also within the particles. This observation suggests that inner-particle cracking can occur under harsh calendering conditions. The maximum yield strength of NCM-based active materials for secondary particles has been reported to be between 100 and 150 MPa.[25,52] To evaluate the potential for crack formation in the active material due to calendering, the crackable volume percentage of the active materials exceeding VMS values of 100–150 MPa was calculated. As summarized in Figure 4b, first, approximately 1.5~5.0 vol% of the active material experiences a VMS level over 100–150 MPa under low compression ratios, such as electrode densities of 2.8 and 3.0 g cm^{-3}. Second, when the electrode density increases to 3.4 or 3.6 g cm^{-3}, the volume percentage increases exponentially to approximately 10 vol% in the base VMS of 100 MPa. Notably, the simulation result supports the experimental data showing that electrodes with densities higher than 3.5 g cm^{-3} exhibited poorer cycle performance (Figure 1b). This implies that particle cracking during calendering may significantly affect cycle performance. Additionally, we developed a protocol to extract the actual crack volume from the reconstructed structures of the actual calendered electrode with a density of 3.6 g cm^{-3} (Figure S11, Supporting Information). Using this protocol, we quantified the actual crack volume and compared it with the crackable volume estimated from a virtually calendered electrode with the same density, where the volume of active material exceeds VMS value of 150 MPa. Figure 4c shows two 3D rendered images: the actual crack volume from the reconstructed structure and the crackable volume from the virtually calendered structure. The size and distribution of the crackable volume within the structure closely resembled the actual crack volume. We calculated the normalized volume percentage between them and plotted it along the electrode thickness, revealing similar curve perturbations (Figure 4d). These results highlight the reliability of VMS-based analysis and its usefulness in diagnosing crack formation during the calendering process. As a point of clarification regarding the correlation between cracked and crackable volumes, it is important to note that they do not share the same physical meaning. To accurately detect the cracked volume in a virtually-calendered structure, an advanced model incorporating the failure and interface properties of the materials, capable of identifying voxels where stress reaches and subsequently drops from the fracture point, is required. This development will be the focus of our future work.

To validate the effectiveness of estimating the geometrical and electrochemical parameters from the digital-twin-driven virtual calendering framework, we constructed a full cell-based pseudo-3D (P3D) model comprising five layers: Al, cathode, separator, anode, and Cu (Figure S12, Supporting Information). The cathode layer was modeled to reflect the actual electrode design parameters with densities ranging from 2.4 to 4.0 g cm^{-3} (Table S2, Supporting Information). Most importantly, in the model, all key geometrical and electrochemical parameters, such as ionic tortuosity, porosity, effective electronic conductivity, effective ionic conductivity effective diffusivity, were derived from the virtual calendering simulation. **Figure** 5a shows the 5C discharge capacity obtained from the experiment and simulation for different electrode densities. The values were highly consistent with a relative error of 6.1%, demonstrating the reliability of the geometrical and electrochemical parameters obtained from the virtual calendering (the corresponding voltage profiles from both the experiment and simulation are presented in Figure S13, Supporting Information). In Figure 5b, the state of lithiation (SOL) at various discharge times is presented as 2D color maps. As shown, the electrode with a density of 3.6 g cm^{-3} maintains more than 27% SOL of active materials across all normalized thicknesses at the end of discharge, whereas the electrode with 3.4 g cm^{-3} never reaches 27% SOL (Figures S14 and S15, Supporting Information). This discrepancy is probably due to the insufficient effective electronic conductivity, as supported by the experimental data. Additionally, the electrode with 3.8 g cm^{-3} shows a sharp change in SOL with increasing normalized electrode thickness, indicating severe polarization along the thickness direction. This result

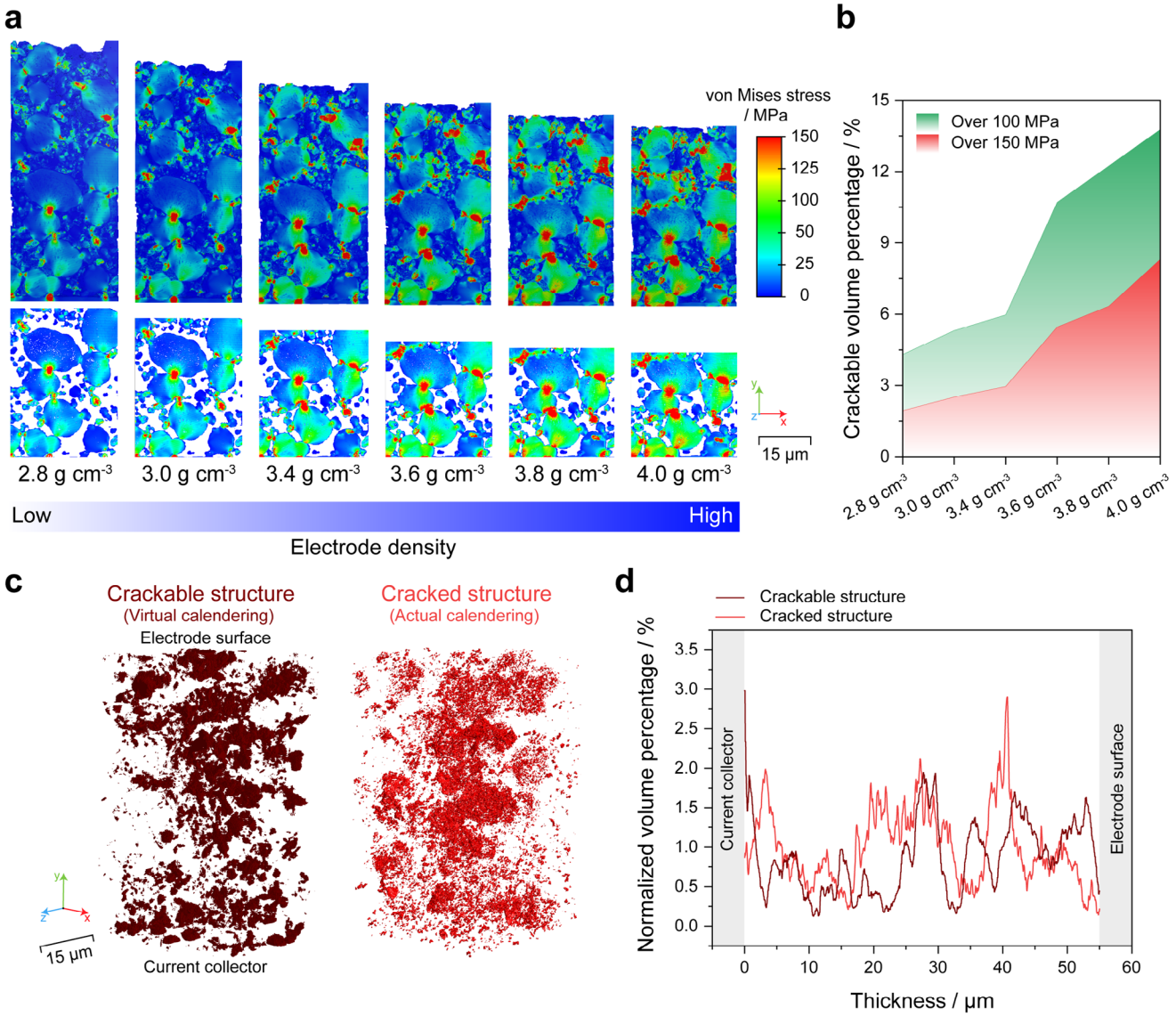

Figure 4. Stress analysis based on the virtual calendering framework. a) von Mises stress (VMS) of the NCM active material during the calendering process to achieve target electrode densities. b) Percentage of NCM volume where particle cracking could potentially occur (crackable), exceeding VMS thresholds of 100 MPa or 150 MPa. c) 3D visualization of the crackable NCM structure and the cracked NCM structure. d) Normalized volume percentage distribution along the electrode thickness direction.

aligns with the prediction from the pore network analysis, which suggests that at an electrode with high density, the lithium-ion concentration gradient would be severe because of the increased tortuosity, smaller pore size, and disconnected pores. Figure 5c shows color maps of the overpotential, electrolyte lithium-ion concentration, and electrolyte potential for different electrode densities at the end of discharge. At a low electrode density, the overpotential values are very high across all normalized thicknesses, exceeding 0.9 V, indicating that a high ohmic overpotential due to low electronic conductivity predominates in electrodes with densities below 2.8 g cm^{-3}. The overpotential decreases with increasing electrode density up to 3.5 g cm^{-3} but increases again after 3.6 g cm^{-3}. This behavior can be attributed to the high electrolyte concentration gradient along the thickness direction of the high-density electrodes. Consistent with this prediction, the electrolyte lithium-ion concentration gradient increases sharply at electrode densities above 3.6 g cm^{-3}, with the liquid potential showing a similar trend. These analyses closely matched and provided a comprehensive explanation for the experimental results shown in Figure 1a. In summary, the electrochemical performance prediction based on a digital twin-driven virtual calendering simulation framework accurately reflects the actual characteristics of the electrodes and can be effectively used to optimize the electrode design, including the electrode density.

Digital twin technology will continue to be applied to various studies on electrode design and its effects, including material composition and distribution, binder morphology, surface modification of particles, functional current collectors or separators,

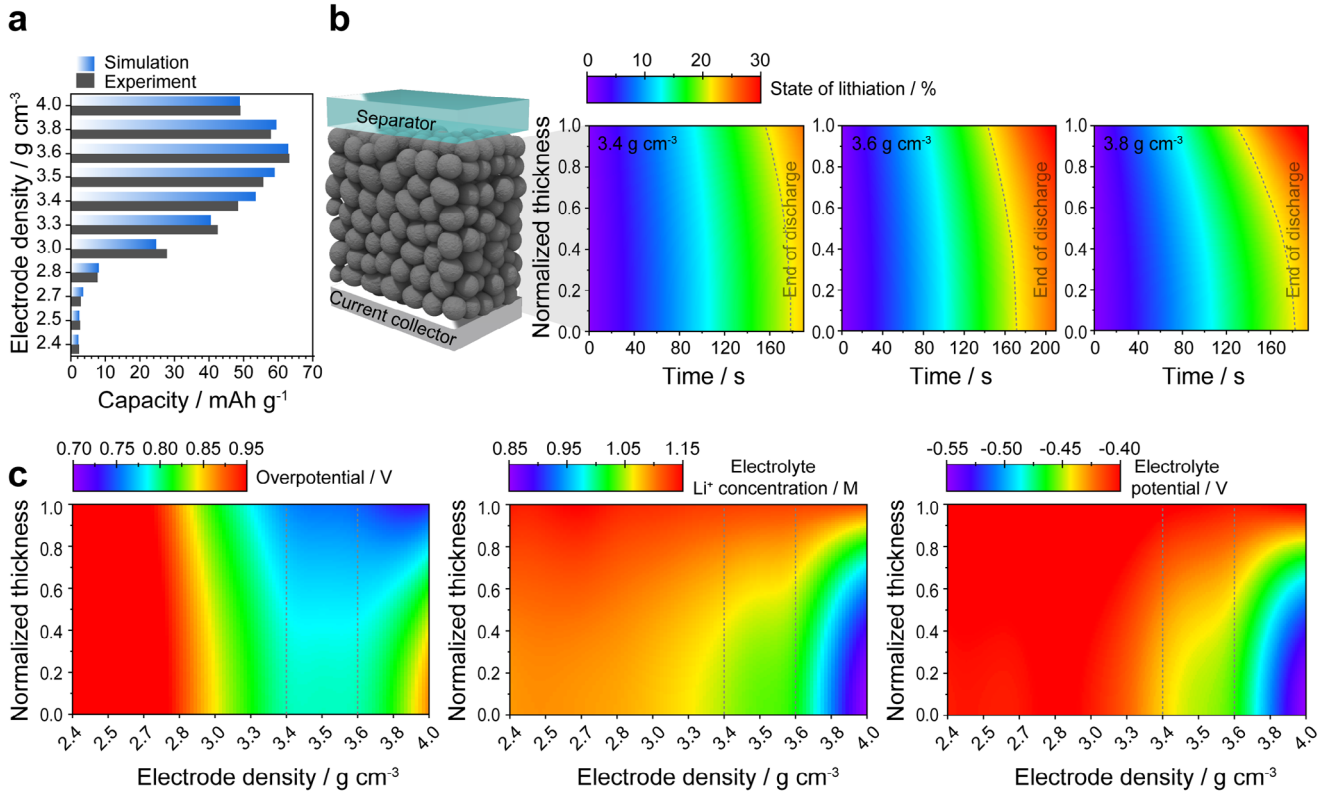

Figure 5. Virtual calendering framework-driven electrochemical performance prediction. a) 5C discharge capacity of Gr||NCM622 full cells with varying cathode densities, evaluated through both experiments and simulations. b) Spatial (across electrode thickness) and temporal distribution of the state of lithiation (SOL) during 5C discharge simulation. c) Spatial distribution of the total overpotential, electrolyte lithium-ion concentration, and electrolyte potential at the end of 5C discharge simulation for different cathode densities.

and particle and electrode deformation, such as crack propagation and volume expansion (**Figure 6**). We aim to identify technical challenges in optimizing electrode design and to develop and report effective research methods using digital twin simulations that can conserve resources and accelerate research.

3. Conclusion

In this study, the correlation between electrode density and electrochemical performance was explored through a digital twin virtual calendaring framework. Experimental and simulation-based analyses were performed at various electrode densities (from 2.4 g cm^{-3} to 4.0 g cm^{-3}) to investigate the effects of the electrode density on the electrode microstructure and electrochemical properties. The best performance was observed when the electrode density was between 3.4 and 3.6 g cm^{-3}, which was evidently supported by high electronic conductivity, sufficient ion transport, enhanced mechanical adhesion, and moderate VMS. The digital twin technology of this study enables precise analysis of these characteristics, utilizing actual electrode structures reconstructed by FIB-SEM tomographic images and the virtual calendaring process which has been proven with experimental data. These results not only provide basic guidelines for optimizing electrode density but are also used to predict electrochemical performance under various electrode design conditions with high reliability. Finally, this digital twin-based research approach will enhance the efficiency of battery research and development and present a new paradigm for generating reliable simulation data.

4. Experimental Section

Electrode Fabrication: To fabricate the composite cathode, a slurry was prepared by the planetary mixing of bimodal $LiNi_{0.6}Co_{0.2}Mn_{0.2}O_2$ (NCM622, purity 99.9%, L&F, Korea) consisting of two particle sizes with a weight ratio of 8:2 (average particle size of large particles: 14 µm; small particles: 3 µm), Super P Super P (Imerys, Switzerland), and polyvinylidene fluoride (PVDF, KF1300, Kureha, Japan) at a weight ratio of 96:2:2 with N-Methyl-2-pyrrolidone (NMP, Sigma-Aldrich, USA). The slurry was cast onto aluminum (Al) foils (15 µm; Sam-A, Republic of Korea) using a doctor blade and dried at 120 °C for 2 h. After drying, the cathode was calendered to target 11 electrode densities from 2.3 g cm^{-3} to 2.4, 2.5, 2.7, 2.8, 3.0, 3.3, 3.4, 3.5, 3.6, 3.8, and 4.0 g cm^{-3}. For all cathodes, the mass loading was controlled to be the same of 19.8 mg cm^{-2} for attaining the same areal capacity (3.42 mAh cm^{-2}). All fabrication processes except the calendering process were conducted in a dry room (dew point ≤ −60 °C).

Cell Assembly: The anode slurry was prepared using artificial graphite (SCMR-AR, Showa Denko, Japan), Super P (Imerys, Switzerland), and a 1:1 mixture of sodium carboxymethyl cellulose (Na-CMC, Dai-ichi Kogyo Seiyaku, Japan) and styrene-butadiene rubber (SBR, BM-400B, Zeon, Japan) in a weight ratio of 96.9:0.5:2.6 with deionized water. The slurry was cast with a doctor blade onto the copper (Cu) foil (10 µm; Iljin Materials, Korea) and dried at 60 °C for 2 h. Then, the anode calendered to the target density of 1.5 g cm^{-3}. The mass loading and areal capacity of anode were 10.46 mg cm^{-2} and 4.26 mAh cm^{-2}, respectively. Thus, the N/P

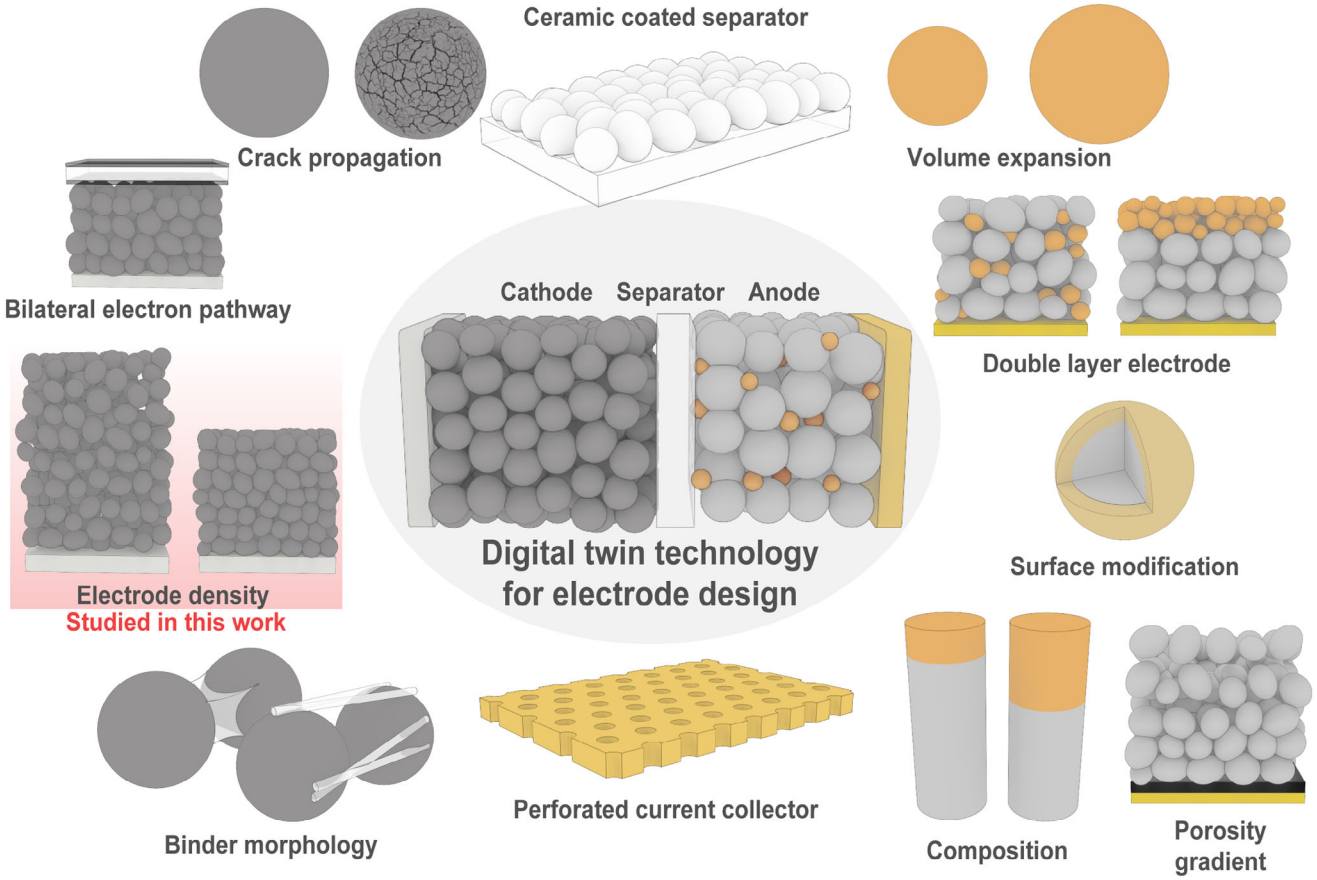

Figure 6. Schematic illustration of various electrode designs.

ratio was ≈1.1. The as-prepared cathodes and anodes were punched into 14 and 16 mm diameter, respectively, and dried in a vacuum oven at 60 °C for 12 h. The 2032 coin-type graphite||NCM622 full cells were assembled in an Ar-filled glove box with 18 mm diameter of polyethylene (PE) separator (F20BHE, 20 µm, Tonen, Japan) and 120 µL liquid electrolyte consisting of 1.15 M lithium hexafluorophosphate ($LiPF_6$) in ethylene carbonate (EC) / ethyl methyl carbonate (EMC) (3/7, v/v) with 2 wt% fluoroethylene carbonate (FEC) additive (Enchem, Rebulic of Korea).

Electrochemical Measurement: Before the electrochemical evaluation, all full cells were aged for 12 h. After aging, a two-step precycling procedure, which included one formation cycle and three stabilization cycles, was conducted to stabilize the cells. During the formation cycle, the cell was charged at a 0.1C in constant current (CC) mode with a 4.3 V cut-off voltage and discharged at the same C-rate with a 3.0 V cut-off voltage. Subsequently, the cell was cycled three times using a 0.2C constant current/constant voltage (CC/CV) charge with a 4.3 V cut-off voltage and a 0.02C cut-off current and discharged at 0.2 a CC with a 3.0 V cut-off voltage. All cycles were conducted at 25 °C using a battery cycler (WBCS3000L, Wonatech, Republic of Korea). For the rate capability test, the discharge rate was controlled from 0.1C to 10C (0.1C, 0.2C, 0.5C, 1C, 2C, 3C, 5C, 10C, and back to 0.1C) in CC mode, while the charge rate was maintained at 0.2C in CC/CV mode. For the cycle test, a 0.5C CC/CV charge and 0.5C CC discharge modes were used. The voltage range was set between 3.0 and 4.3 V for both the rate capability and cycle tests.

Electrode Characterization: An electrode resistance measurement system (RM2610, HIOKI, Japan) was used to measure the electronic resistivity of the electrodes. The measurements were conducted in the current range of 0–1 mA and voltage range of 0–0.5 V. A surface and interfacial cutting analysis system (SAICAS, SAICAS-DN, Daipla Wintes, Japan) was used to measure the adhesion strength of the electrodes. The adhesion strength within the electrode was repeatedly measured five times in the middle of the electrode thickness using a boron nitride blade (width: 1 mm) at a horizontal speed of 2 µm s^{-1}.

Formation of a 3D Digitally Twined Structure from FIB-SEM Tomographic Images: A substantial dataset comprising thousands of cross-sectional images was acquired using a focused ion beam scanning electron microscopy (FIB-SEM) system (Crossbeam 550, ZEISS, Germany). For the uncalendared electrode, 1500 FIB-SEM cross-sectional images were obtained with a pixel resolution of 37.22 nm and an ion milling interval of 32.5 nm, resulting in a domain size of approximately 30 × 90 × 40 μm^3 (width × thickness × depth). Subsequently, for the electrode calendared to a density of 3.6 g cm^{-3}, 1160 cross-sectional SEM images were obtained, featuring a pixel size of 42.94 nm and the same ion milling interval, leading to a domain size of approximately 33 × 60 × 56 μm^3. The FIB-SEM tomographic images were then processed with a fast Fourier transform filter and a nonlocal means filter using GeoDict software (Math2Market, Germany). The images were rescaled and processed using a trilinear scale function along the ion milling direction (z-direction). Segmentation was performed using the gray-value threshold method and a watershed algorithm, which facilitated the construction of a 3D digitally twined electrode structure based on the segmented images.

Calendering Process Modeling and Simulation: With the reconstructed uncalendared electrode, calendering (or deformation) simulations were conducted to construct virtual electrode structures with the targeted densities using the ElastoDict module in GeoDict 2023, which is based on the finite-volume method (FVM).[53–57] All materials were assumed to be linearly elastic, and calendering was modeled as a uniaxial compression process in the thickness direction (y-direction). Detailed modeling

parameters and governing equations are provided in the Supporting Information. Symmetric boundary conditions were applied, and the mechanical load was set as strain-controlled, meaning that the deformation simulation was terminated depending on the thickness or strain of electrodes with the target density. Based on the targeted strain values, linear elastic material model, governing equations, and boundary conditions, the displacement field of each voxel or element was computed, and as a result, the voxels were repositioned. This resampling process ensured that the total volume was maintained and that no loss of the total volume of the solid material occurred.[58]

Analysis of 3D Digitally Twined Electrode Structures: Using the DiffuDict module in GeoDict 2023, the effective diffusion coefficient ($D_{e,eff}$) was calculated using the reconstructed or virtually calendered digital twin structures. The boundary conditions were set as $\Delta C = 1$ mol m^{-3} for the $D_{e,eff}$ calculations under the Dirichlet condition along the electrode thickness direction (y-direction), applying a constant concentration value on the normal planes (*x*–*z* planes). Fick's law was used as the governing equation for the $D_{e,eff}$ calculations. The intrinsic diffusion coefficient of the liquid electrolyte, 1.15 M $LiPF_6$ in EC/EMC (3/7, v/v) (D_e) at 298.15 K was set as an input parameter using an FVM-based solver for calculating the diffusion flux (J). Additionally, utilizing the relationship between volume fraction (ϵ_e), intrinsic diffusion coefficient (D_e), tortuosity (τ_e), and effective diffusion coefficient ($D_{e,eff}$) (Equation 1), the tortuosity of the pore domain was estimated.[59–61]

$$D_{e,eff} = \frac{\epsilon_e}{\tau_e^2} D_e \tag{1}$$

where $D_{e,eff}$, ϵ_e, τ_e, and D_e are the effective diffusion coefficient, volume fraction, tortuosity, and intrinsic diffusion coefficient of the electrolyte or pore domain, respectively (lower subscript e indicates the "electrolyte" domain.).

The ConductoDict module in GeoDict 2023 was used to calculate electronic conductivity. A Dirichlet boundary condition with $\Delta V = 1$ V was applied, and Ohm's law was defined as the governing equation. Similar to the diffusion coefficient calculation, an FVM-based solver was used to calculate the current density. The electronic conductivity of each digital twin structure was estimated based on the estimated current density and governing equation.

Pore Network Analysis: 3D digital twin structures from calendering simulations and open-source MATLAB (MathWorks, USA) code were employed for the pore network model (PNM)-based analysis.[62] A watershed algorithm was used to distinguish each pore. Each pore was numbered as pore index based on Cartesian coordinates and the connectivity between the pores was determined, yielding a coordination number and pore connectivity matrix. Statistical analyses were conducted using the connectivity matrix to compare the pore connectivity within the digital twin structures with different geometrical domain sizes. First, each connection point in the connectivity matrix is orthogonally projected onto the line $y = x$, which is the line normal to the diagonal of the connectivity matrix. Subsequently, all projected points were normalized to the range (−1, 1) for relative comparison. Finally, the probability density function (PDF) was calculated, and the standard deviation was determined.

Electrochemical Modeling and Simulation: An electrochemical model for the discharge simulation was developed for the graphite||NCM622 full cell using COMSOL Multiphysics 6.1 (COMSOL. USA). Based on Doyle and Newman's approach,[63] the model was built on a pseudo-three-dimensional (P3D) domain with Cartesian dimensions x and y, and a pseudo-dimension r. In the model, the actual dimensions of the composite electrodes and electrochemical properties of each cathode were incorporated, which corresponded to the digital twin structures obtained from the calendering simulation. The model comprised an Al current collector, an NCM622 electrode, a separator, a graphite electrode, and a Cu current collector. Governing equations, including charge conservation, electroneutrality, mass conservation, Fick's law, Ohm's law, and Butler–Volmer equations were assigned to each component. The governing equations, boundary conditions, and electrochemical parameters are summarized in Tables S3 and S4 (Supporting Information). Finally, electrochemical simulations were performed under constant current discharge conditions with a 5 C rate and a 3.0 V cut-off using a multifrontal massively parallel sparse direct solver (MUMPS). The control volume size was 30 µm × L_y × 40 µm, where L_y represents the total cell length, including the Al current collector, cathode, separator, anode, and Cu current collector (as detailed in Figure S9 and Table S2, Supporting Information). The simulations were performed with a time step of 5 s.

Supporting Information

Supporting Information is available from the Wiley Online Library or from the author.

Acknowledgements

J.L. and J.S. contributed equally to this work. This work was supported by the National Research Foundation of Korea (NRF) grant funded by the Korean government (MSIT) (No. NRF-2021M3H4A1A02048529) and LG Energy Solution, Ltd. The authors are also grateful for the support from the DGIST Supercomputing and Big Data Center.

Conflict of Interest

The authors declare no conflict of interest.

Data Availability Statement

The data that support the findings of this study are available from the corresponding author upon reasonable request.

Keywords

Digital Twin, Electrode density, microstructure, Modeling and Simulation, Virtual calendering process

Received: November 6, 2024
Revised: January 27, 2025
Published online:

[1] O. Gröger, H. A. Gasteiger, J.-P. Suchsland, *J. Electrochem. Soc.* **2015**, *162*, A2605.
[2] R. Sim, S. Lee, W. Li, A. Manthiram, *ACS Appl. Mater. Interfaces* **2021**, *13*, 42898.
[3] E. N. Primo, M. Chouchane, M. Touzin, P. Vazquez, A. A. Franco, *J. Power Sources* **2021**, *488*, 229361.
[4] M. Abdollahifar, H. Cavers, S. Scheffler, A. Diener, M. Lippke, A. Kwade, *Adv. Energy Mater.* **2023**, *13*, 2300973.
[5] J. Gnanaraj, Y. S. Cohen, D. Aurbach, *J. Electroanal. Chem.* **2001**.
[6] A. van Bommel, R. Divigalpitiya, *J. Electrochem. Soc.* **2012**, *159*, A1791
[7] V. Murray, D. S. Hall, J. R. Dahn, *J. Electrochem. Soc.* **2019**, *166*, A329.
[8] C. Meyer, M. Weyhe, W. Haselrieder, A. Kwade, *Energy Technol.* **2020**, *8*, 1900175.
[9] T. Günther, D. Schreiner, A. Metkar, C. Meyer, A. Kwade, G. Reinhart, *Energy Technol.* **2020**, *8*, 1900026.
[10] D. Schmidt, M. Kamlah, V. Knoblauch, *J. Energy Storage* **2018**, *17*, 213.
[11] M. Jiang, D. L. Danilov, R. A. Eichel, P. H. L. Notten, *Adv. Energy Mater.* **2021**, *11*, 2103005 .

[12] S. Lee, W. Li, A. Dolocan, H. Celio, H. Park, J. H. Warner, A. Manthiram, *Adv. Energy Mater.* **2021**, *11*, 2100858.
[13] J. K. Morzy, W. M. Dose, P. E. Vullum, M. C. Lai, A. Mahadevegowda, M. F. L. De Volder, C. Ducati, *ACS Appl. Energy Mater.* **2024**, *7*, 3945.
[14] S. Lee, L. Su, A. Mesnier, Z. Cui, A. Manthiram, *Joule* **2023**, *7*, 2430.
[15] G. J. Páez Fajardo, E. Fiamegkou, J. A. Gott, H. Wang, I. Temprano, I. D. Seymour, M. J. W. Ogley, A. S. Menon, I. E. L. Stephens, M. Ans, T. L. Lee, P. K. Thakur, W. M. Dose, M. F. L. De Volder, C. P. Grey, L. F. J. Piper, *ACS Energy Lett.* **2023**, *8*, 5025.
[16] T. M. M. Heenan, A. Wade, C. Tan, J. E. Parker, D. Matras, A. S. Leach, J. B. Robinson, A. Llewellyn, A. Dimitrijevic, R. Jervis, P. D. Quinn, D. J. L. Brett, P. R. Shearing, *Adv. Energy Mater.* **2020**, *10*, 2002655.
[17] E. N. Primo, M. Touzin, A. A. Franco, *Batter. Supercaps* **2021**, *4*, 834.
[18] I. Bloom, B. W. Cole, J. J. Sohn, S. A. Jones, E. G. Polzin, V. S. Battaglia, G. L. Henriksen, C. Motloch, R. Richardson, T. Unkelhaeuser, D. Ingersoll, H. L. Case, *J. Power Sources* **2001**, *101*, 238.
[19] D. Schreiner, M. Oguntke, T. Günther, G. Reinhart, *Energy Technol.* **2019**, *7*, 1900840.
[20] B. L. Trembacki, D. R. Noble, M. E. Ferraro, S. A. Roberts, *J. Electrochem. Energy Conversion Storage* **2020**, *17*, 14.
[21] C. Meyer, H. Bockholt, W. Haselrieder, A. Kwade, *J. Mater. Process. Technol.* **2017**, *249*, 172.
[22] S. Oswald, D. Pritzl, M. Wetjen, H. A. Gasteiger, *J. Electrochem. Soc.* **2020**, *167*, 100511.
[23] C. F. Oladimeji, P. L. Moss, M. H. Weatherspoon, *Adv. Chem.* **2016**, *2016*, 1.
[24] J. Lee, S. Byun, H. Lee, Y. Roh, D. Jin, J. Lim, J. Song, C. B. Dzakpasu, J. Park, Y. M. Lee, *Battery Energy* **2023**, *2*, 20220061.
[25] J. Song, S. H. Lim, K. G. Kim, N. Umirov, H. Lee, C. B. Dzakpasu, J. Lim, J. Nam, J. Park, J. N. Lee, H. Munakata, K. Kanamura, S. S. Kim, Y. M. Lee, *Adv. Energy Mater.* **2023**, *13*, 2204328.
[26] J. Song, J. Park, W. A. Appiah, S. S. Kim, H. Munakata, K. Kanamura, M. H. Ryou, Y. M. Lee, *Nano Energy* **2019**, *62*, 810.
[27] J. Park, K. T. Bae, D. Kim, W. Jeong, J. Nam, M. J. Lee, D. O. Shin, Y. G. Lee, H. Lee, K. T. Lee, Y. M. Lee, *Nano Energy* **2021**, *79*, 105456.
[28] S. R. Daemi, X. Lu, D. Sykes, J. Behnsen, C. Tan, A. Palacios-Padros, J. Cookson, E. Petrucco, P. J. Withers, D. J. L. Brett, P. R. Shearing, *Mater. Horiz.* **2019**, *6*, 612.
[29] M. Ebner, D. W. Chung, R. E. García, V. Wood, *Adv. Energy Mater.* **2014**, *4*, 1301278.
[30] D. E. Stephenson, B. C. Walker, C. B. Skelton, E. P. Gorzkowski, D. J. Rowenhorst, D. R. Wheeler, *J. Electrochem. Soc.* **2011**, *158*, A781.
[31] M. Ebner, F. Geldmacher, F. Marone, M. Stampanoni, V. Wood, *Adv. Energy Mater.* **2013**, *3*, 845.
[32] G. Lenze, F. Röder, H. Bockholt, W. Haselrieder, A. Kwade, U. Krewer, *J. Electrochem. Soc.* **2017**, *164*, A1223.
[33] A. M. Boyce, E. Martínez-Pañeda, A. Wade, Y. S. Zhang, J. J. Bailey, T. M. M. Heenan, D. J. L. Brett, P. R. Shearing, *J. Power Sources* **2022**, *526*, 231119 .
[34] J. Park, K. T. Kim, D. Y. Oh, D. Jin, D. Kim, Y. S. Jung, Y. M. Lee, *Adv. Energy Mater.* **2020**, *10*, 2001563.
[35] M. Zhang, M. Chouchane, S. A. Shojaee, B. Winiarski, Z. Liu, L. Li, R. Pelapur, A. Shodiev, W. Yao, J. M. Doux, S. Wang, Y. Li, C. Liu, H. Lemmens, A. A. Franco, Y. S. Meng, *Joule* **2023**, *7*, 201.
[36] J. Scharf, M. Chouchane, D. P. Finegan, B. Lu, C. Redquest, M. cheol Kim, W. Yao, A. A. Franco, D. Gostovic, Z. Liu, M. Riccio, F. Zelenka, J. M. Doux, Y. S. Meng, *Nat. Nanotechnol.* **2022**, *17*, 446.
[37] X. Lu, S. R. Daemi, A. Bertei, M. D. R. Kok, K. B. O'Regan, L. Rasha, J. Park, G. Hinds, E. Kendrick, D. J. L. Brett, P. R. Shearing, *Joule* **2020**, *4*, 2746.
[38] R. Ge, A. M. Boyce, Y. Shui Zhang, P. R. Shearing, D. J. Cumming, R. M. Smith, *Chem. Eng. J.* **2023**, *465*, 142749.
[39] J. Xu, B. Paredes-Goyes, Z. Su, M. Scheel, T. Weitkamp, A. Demortière, A. A. Franco, *Batter Supercaps* **2023**, *6*, 202300371.
[40] J. Xu, A. C. Ngandjong, C. Liu, F. M. Zanotto, O. Arcelus, A. Demortière, A. A. Franco, *J. Power Sources* **2023**, *554*, 232294.
[41] C. Liu, T. Lombardo, J. Xu, A. C. Ngandjong, A. A. Franco, *Energy Storage Mater.* **2023**, *54*, 156.
[42] V. Baric, L. C. Ciacchi, L. Mädler, *Powder Technol.* **2019**, *342*, 773.
[43] M. Nikpour, N. Barrett, Z. Hillman, A. I. Thompson, B. A. Mazzeo, D. R. Wheeler, *J. Electrochem. Soc.* **2021**, *168*, 060547.
[44] A. C. Ngandjong, T. Lombardo, E. N. Primo, M. Chouchane, A. Shodiev, O. Arcelus, A. A. Franco, *J. Power Sources* **2021**, *485*, 229320.
[45] J. Landesfeind, J. Hattendorff, A. Ehrl, W. A. Wall, H. A. Gasteiger, *J. Electrochem. Soc.* **2016**, *163*, A1373.
[46] N. Ogihara, Y. Itou, T. Sasaki, Y. Takeuchi, *J. Phys. Chem. C* **2015**, *119*, 4612.
[47] N. Ogihara, S. Kawauchi, C. Okuda, Y. Itou, Y. Takeuchi, Y. Ukyo, *J. Electrochem. Soc.* **2012**, *159*, A1034.
[48] H. Lee, S. Yang, S. Kim, J. Song, J. Park, C. H. Doh, Y. C. Ha, T. S. Kwon, Y. M. Lee, *Curr. Opin. Electrochem.* **2022**, *34*, 100986.
[49] N. Saxena, R. Hofmann, F. O. Alpak, S. Berg, J. Dietderich, U. Agarwal, K. Tandon, S. Hunter, J. Freeman, O. B. Wilson, *Adv. Water Resour.* **2017**, *109*, 211.
[50] N. Saxena, A. Hows, R. Hofmann, F. O. Alpak, J. Freeman, S. Hunter, M. Appel, *Adv. Water Resour.* **2018**, *116*, 127.
[51] K. Yang, X. Xie, X. Du, Y. Zuo, Y. Zhang, *Processes* **2023**, *11*, 1800.
[52] R. Xu, Y. Yang, F. Yin, P. Liu, P. Cloetens, Y. Liu, F. Lin, K. Zhao, *J. Mech. Phys. Solids* **2019**, *129*, 160.
[53] J. T. Browaeys, S. Chevrot, *Geophys. J. Int.* **2004**, *159*, 667.
[54] M. Schneider, F. Ospald, M. Kabel, *Int. J. Numer. Methods Eng.* **2016**, *105*, 693.
[55] M. Kabel, S. Fliegener, M. Schneider, *Comput. Mech.* **2016**, *57*, 193.
[56] H. Grimm-Strele, M. Kabel, *Comput. Mech.* **2019**, *64*, 1339.
[57] V. Rutka, A. Wiegmann, *Numer. Algorithms* **2006**, *43*, 309.
[58] M. Kabel, D. Merkert, M. Schneider, *Comput. Methods Appl. Mech. Eng.* **2015**, *294*, 168.
[59] B. P. Boudreau, *Geochim. Cosmochim. Acta* **1996**, *60*, 3139.
[60] P. Moldrup, T. Olesen, T. Komatsu, P. Schjønning, D. E. Rolston, *Soil Sci. Soc. Am. J.* **2001**, *65*, 613.
[61] B. Tjaden, D. P. Finegan, J. Lane, D. J. L. Brett, P. R. Shearing, *Chem. Eng. Sci.* **2017**, *166*, 235.
[62] A. Rabbani, S. Jamshidi, S. Salehi, *J. Pet. Sci. Eng.* **2014**, *123*, 164.
[63] M. Doyle, J. Newman, A. S. Gozdz, C. N. Schmutz, J.-M. Tarascon, *J. Electrochem. Soc.* **1996**, *143*, 1890.